Template-Assisted Low Temperature Synthesis of Functionalized Graphene for Ultrahigh Volumetric Performance Supercapacitors

Jun Yan,[†] Qian Wang,[†] Tong Wei, Lili Jiang, Milin Zhang, Xiaoyan Jing, and Zhuangjun Fan*

Key Laboratory of Superlight Materials and Surface Technology, Ministry of Education, College of Material Science and Chemical Engineering, Harbin Engineering University, Harbin 150001, China. [†]J. Yan and Q. Wang contributed equally to this work.

ABSTRACT We demonstrated the fabrication of functionalized graphene nanosheets *via* low temperature (300 °C) treatment of graphite oxide with a slow heating rate using $Mg(OH)_2$ nanosheets as template. Because of its dented sheet with high surface area, a certain amount of oxygen-containing groups, and low pore volume, the as-obtained graphene delivers both ultrahigh specific gravimetric and volumetric capacitances of 456 F g^{-1} and 470 F cm^{-3}, almost 3.7 times and 3.3 times higher than hydrazine reduced graphene, respectively. Especially, the obtained volumetric capacitance is the highest value so far reported for carbon materials in aqueous electrolytes. More importantly, the assembled supercapacitor exhibits an ultrahigh volumetric energy density of 27.2 Wh L^{-1}, which is among the highest values for carbon materials in aqueous electrolytes, as well as excellent cycling stability with 134% of its initial capacitance after 10 000 cycles. Therefore, the present work holds a great promise for future design and large-scale production of high performance graphene electrodes for portable energy storage devices.

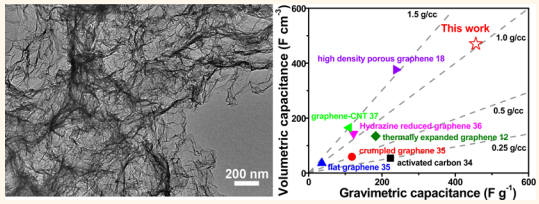

KEYWORDS: template-assisted synthesis · supercapacitors · graphene · high volumetric performance

Because of their ultralong cycling stability and high power density, supercapacitors have received considerable attention in potential applications such as portable electronics, electric vehicles, and so on.[1−3] Recently, graphene, with an extremely high theoretical surface area (2630 m^2 g^{-1}) and a superior theoretical capacitance of 550 F g^{-1}, has been considered as an ideal electrode material for supercapacitors.[4−6] However, chemically reduced graphene oxide produced on a large scale at low cost often suffers from irreversible sheet-to-sheet restacking due to the strong interlayer van der Waals force, resulting in the deterioration of its high specific surface area and subsequent decrease of the specific capacitance. To fully utilize and further explore new functions of graphene sheets, considerable investments have been performed to design out-of-plane space by introducing "spacer" between graphene layers (such as carbon nanotubes, metal oxides, metal hydroxides, and conducting polymers) or by introducing more crumples/pores on the sheets,[7−10] which would significantly improve electrolyte accessible surface area of graphene, resulting in enhanced electrochemical performance.

Thermal exfoliation of graphene oxide is conceived to be an environmentally friendly synthesis method in which no hazardous reductant is used compared with chemical reduction method. This process requires a rapid heating of graphite oxide (GO) at high temperatures up to 800 °C or a low temperature in a high vacuum environment to promote the expansion of graphene sheets.[11−14] On the contrary, the slow heating rate usually causes the serious restacking of graphene sheets no matter at low or high temperatures, resulting in the dense structures with low specific surface area, which is disadvantageous for energy storage in practical applications.

Recently, tremendous achievements have been made in improving the gravimetric capacitances of graphene-based supercapacitors through different approaches.[7−9,15] However, the volumetric performances are mostly ignored regrettably. Because graphene with high surface area has a large

* Address correspondence to fanzhj666@163.com.

Received for review January 25, 2014 and accepted April 14, 2014.

Published online April 14, 2014
10.1021/nn500497k

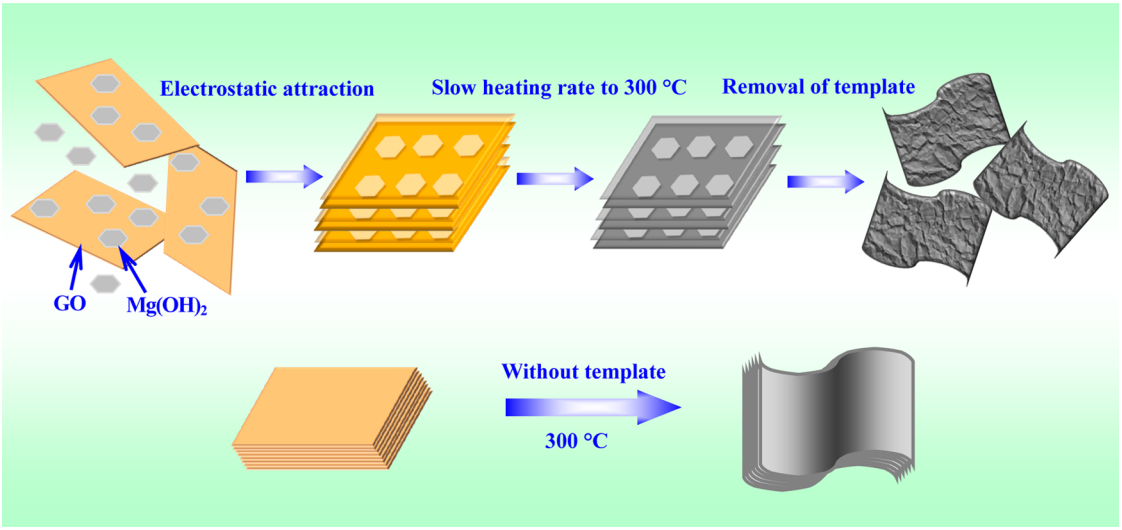

Figure 1. Schematic illustration of the fabrication of FGN-300.

pore volume and low particle density, its volumetric capacitance is often rather low, which is unfavorable for the practical applications in the future. Therefore, electrode materials with both high gravimetric and volumetric capacitances are urgently required for future application in portable energy storage devices where space is relatively limited. Nowadays, many efforts have been performed to fabricate the high volumetric density graphene, MXene, and other materials.[16−19]

Here, we developed a novel strategy to synthesize rationally functionalized graphene sheets (FGN-300) *via* low temperature (300 °C) thermal reduction of GO with a slow heating rate under the assistance of $Mg(OH)_2$ template, as shown in Figure 1. First, $Mg(OH)_2$ nanosheets are introduced in-between GO sheets to prevent the graphene sheets from restacking/agglomeration as "spacers" during the heat-treatment of GO, ensuring high surface area for graphene sheets. Second, $Mg(OH)_2$ nanosheets as template were impressed on GO to form footprint-like structure after their removal. Third, there are large amounts of stable oxygen-containing groups remaining on graphene sheet due to low temperature treatment of GO, providing more pseudocapacitance. Finally, it is very hard to expand for the graphene sheets due to the slow heating rate, resulting in low pore volume and high powder density. Consequently, it exhibits both ultrahigh specific gravimetric and volumetric capacitances of 456 F g^{-1} and 470 F cm^{-3}, almost 3.7 times and 3.3 times higher than hydrazine reduced graphene oxide (RGO), respectively. More importantly, FGN-300 symmetric supercapacitor delivers an ultrahigh volumetric energy density of 27.2 Wh L^{-1} in an aqueous electrolyte, higher than most reported values for carbon based supercapacitors.

RESULTS AND DISCUSSION

In this work, GO was synthesized by the modified Hummers method from natural graphite (Qingdao Graphite Company).[9] GO exhibits a typical flat and smooth flake-like morphology with the lateral size ranging from several tens of nanometers to a few micrometers and the thickness of ~1 nm (Figure S1, Supporting Information). In a typical synthesis of FGN-300, the as-prepared $Mg(OH)_2$ (2 g) was dispersed in 200 mL of distilled water, and the GO dispersion (100 mg, 0.5 mg mL^{-1}) was added dropwise into the above solution after ultrasonication for 1 h. GO suspension with a concentration of 0.5 mg mL^{-1} is rather stable (Figure 2a-1) with a high zeta potential (−30 mV) coming from the presence of numerous oxygen containing functional groups.[20] Similarly, $Mg(OH)_2$ nanosheets with a positive zeta potential possess the size of 80−100 nm (Figure S2a,b, Supporting Information), and once it is mixed with GO together, flocculent precipitate is generated immediately because of the electrostatic attraction (Figure 2a-2). After thermal treatment, FGN-300 exhibits a much larger volume than the sample without $Mg(OH)_2$ template (named TRG) with the same weight (Figure 2b), suggesting that the $Mg(OH)_2$ nanosheets effectively prevent the restacking/agglomeration of graphene sheets as "spacers". Scanning electron microscopy (SEM) image of TRG shows a dense and compact layered structure (Figure 2c). When $Mg(OH)_2$ template is introduced into the system, $Mg(OH)_2$ nanosheets can be successfully absorbed on the surface of GO sheets (Figure 2d). After thermal treatment at 300 °C for 2 h, the FGN-300 exhibits a distinctly crumpled morphology (Figure 2e), also demonstrating the important role of $Mg(OH)_2$ as "spacers" in preventing the restacking of graphene sheets. Moreover, a highly dented surface is also confirmed by transmission electron microscopy (TEM) observation (Figure 2f). High-magnification TEM image (Figure 2g) further demonstrates that there are numerous "footprints" on the surface of sheets due to the presence of $Mg(OH)_2$ as template. These concave regions can serve as ion-buffering reservoirs, which can

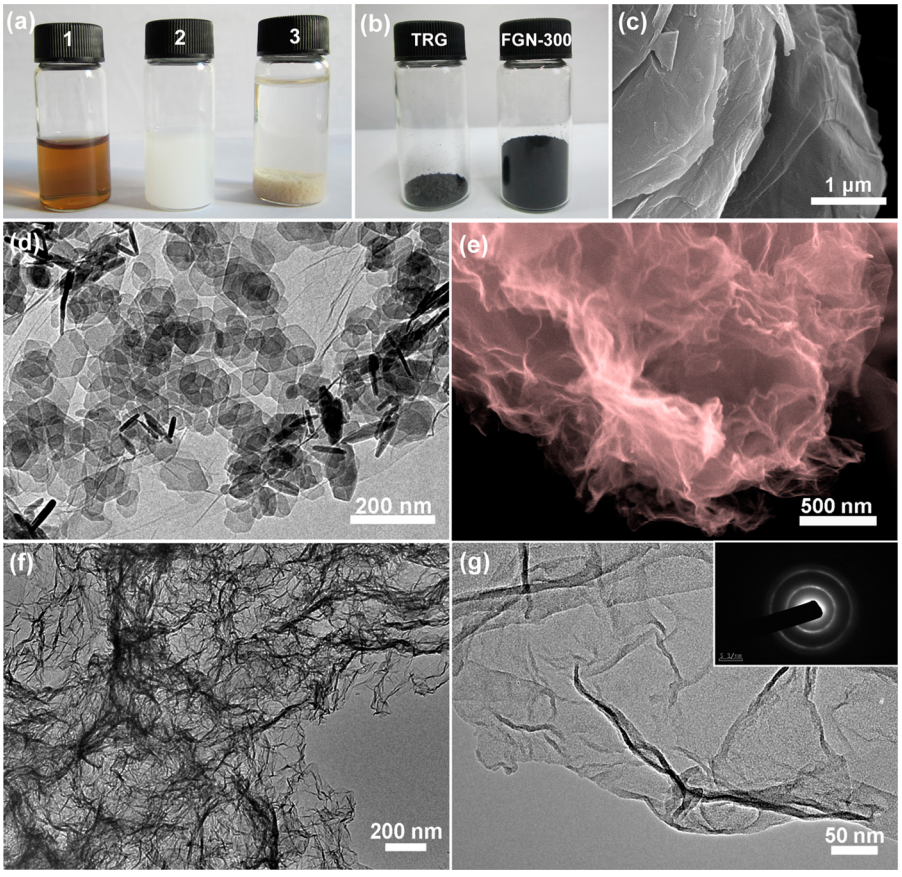

Figure 2. Digital photos of (a) GO, $Mg(OH)_2$ suspension, the mixture of GO and $Mg(OH)_2$ and (b) the powder of TRG and FGN-300. (c) SEM image of TRG. (d) TEM image of $Mg(OH)_2$/GO mixture. SEM (e) and TEM (f,g) of the FGN-300 (inset: SAED of FGN-300).

provide a short diffusion distance and facilitate the rapid transport of electrolyte ions to the interior of graphene layers. Moreover, selected area electron diffraction (SAED) exhibits a bright diffraction ring assigned to the (100) reflection plane of graphene (inset of Figure 2g), indicating that the conjugated structure of graphitic domains in GO is partially recovered after thermal treatment.[13]

The powder X-ray diffraction (XRD) was further used to analyze the bulk structure of the samples. There is a sharp (001) diffraction peak around $2\theta = 10°$ for GO (Figure 3a). After the thermal treatment of GO, a new sharp peak (002) centered at 24° appears for TRG, whereas the broader and weaker (002) peak for FGN-300 reveals a highly disordered restacking of sheets, demonstrating a loose structure. N_2 adsorption−desorption isotherm of FGN-300 exhibits type IV with a distinct hysteresis loop of type H3 at a relative pressure p/p_0 ranging from 0.5 to 1.0 (Figure 3b), indicating the existence of mesopores (Figure S3a, Supporting Information). Because of its dense structure, TRG has an extremely low Brunauer−Emmett−Teller specific surface area (BET, SSA) of 19 $m^2\ g^{-1}$, indicating that almost no exfoliation occurred during the thermal treatment process, while the BET SSA of FGN-300 is significantly increased to 285 $m^2\ g^{-1}$ (pore volume: 0.47 $cm^3\ g^{-1}$) because of the introduction of $Mg(OH)_2$ effectively preventing the restacking/agglomeration of graphene sheets as "spacers". Additionally, Raman analysis exhibits that I_D/I_G ratio of FGN-300 is 1.52 (Figure 3c), indicating that there are a large amount of defects remaining on sheets, which may be attributed to the decrease in the average size of the sp^2 graphene domains and the loss of carbon atoms by the decomposition of oxygen-containing functional groups.[21,22] The thermal stability of FGN-300 and GO were measured using thermogravimetric analysis (TGA, Figure 3d). As for GO, a small weight loss (10%) around 100 °C is related to the elimination of adsorbed water. After that, there is 40% weight loss at around 300 °C corresponding to the pyrolysis of the labile oxygen-containing functional groups, especially the decomposition of hydroxyl and lactone groups. However, only 7.2% weight loss occurred for FGN-300 sample at around 700 °C, demonstrating that the remaining oxygen-containing functionalities are stable.

To investigate the effect of the treatment temperature on the content of oxygen-containing functionalities, we also performed a series of experiments for comparison. Fourier transform infrared (FT-IR) and X-ray photoemission spectroscopy (XPS) were used to characterize the chemical structure and composition of the samples (Figure 4). The intense absorption bands centered at 1643 and 1380 cm^{-1} are related to

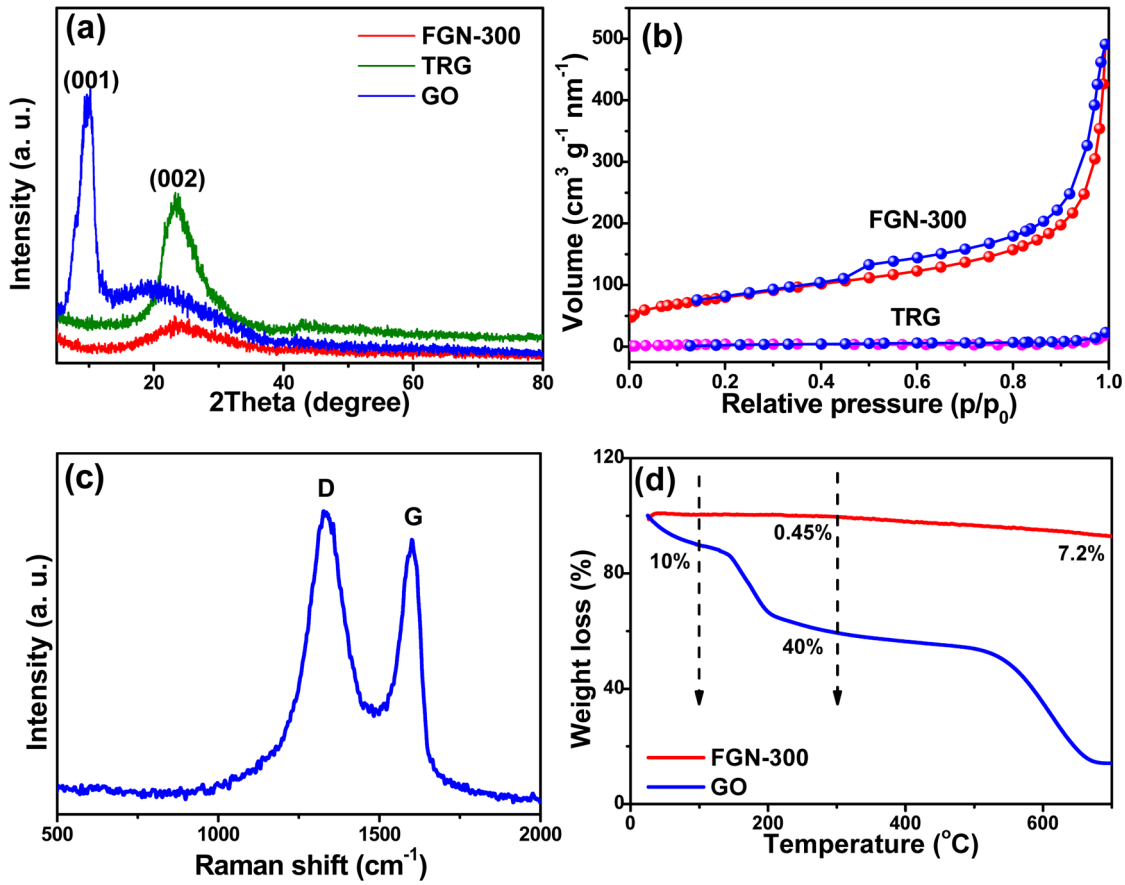

Figure 3. (a) XRD patterns of GO, TRG, and FGN-300 samples. (b) N_2 adsorption isotherms of TRG and FGN-300. (c) Raman spectrum of FGN-300. (d) TGA profile of GO and FGN-300.

the stretching vibration of C═O and C−O in COOH groups, respectively, and the bands centered at 1320 and 1110 cm^{-1} are assigned to the C−OH stretching vibration, C−O stretching vibration in C−O−C, respectively (Figure 4a).[23,24] After the thermal treatment of GO, the intensity of these peaks for the oxygen-containing functionalities is obviously weakened, demonstrating the partial reduction of GO. The quantitative characterizations of the remaining oxygen-containing functionalities were performed using XPS analysis. The C 1s spectra of the samples are shown in Figure 4b−d, and the five different peaks centered at 284.5, 285.6, 286.7, 287.9, and 290.3 eV can be attributed to the sp^2 C, sp^3 C, C−O, C═O, and O═C—O group, respectively.[13] Notably, the percentage of sp^2 carbon increases remarkably from 37.27 to 53.53% after the thermal treatment of GO at 300 °C (Table S1, Supporting Information), indicating that the conjugated graphene networks are restored after heat treatment. Furthermore, the percentage of C−O and O═C—O for FGN-300 still remains 6.85 and 12.99%, respectively, indicating large amounts of oxygen-containing functional groups remained on graphene sheets. Significantly, the atom ratio of O/C decreases from 0.20 to 0.06 with the increase of the temperature from 300 to 800 °C, meaning that the oxygen-containing functionalities can be efficiently removed after high temperature treatment of GO. This can be also confirmed by the improved electrical conductivity for FGN-800 (46 S m^{-1}) compared to FGN-300 (2.9 S m^{-1}) and FGN-650 (17 S m^{-1}). More interestingly, apart from oxygen-containing functionalities, there is no obvious change of bulk volume and SSA for FGN-300 (285 m^2 g^{-1}), FGN-650 (308 m^2 g^{-1}), and FGN-800 (319 m^2 g^{-1}) samples (Figure S3a,b, Supporting Information), meaning that the use of $Mg(OH)_2$ template and low thermal temperature can ensure the as-prepared sample with both a high SSA and a certain amount of stable oxygen-containing functionalities. In addition, the O/C ratio of FGN-300 is higher than those of thermal exfoliated graphene sheet (TEGS, 0.15) and RGO (0.16), as shown in Figure S4 and Table S1 (Supporting Information).

As expected, FGN-300 has a crumpled structure with a high surface area and large amounts of stable oxygen-containing functionalities, which would be beneficial for high performance supercapacitors. The electrochemical performances of the FGN-300, FGN-650, and FGN-800 electrodes were first investigated by cyclic voltammetry (CV, Figure 5). Obviously, the FGN-800 electrode has a nearly rectangle shape, meaning that its capacitance mainly comes from electrical double layer capacitance (EDLC). As for the FGN-300 electrode, its capacitance

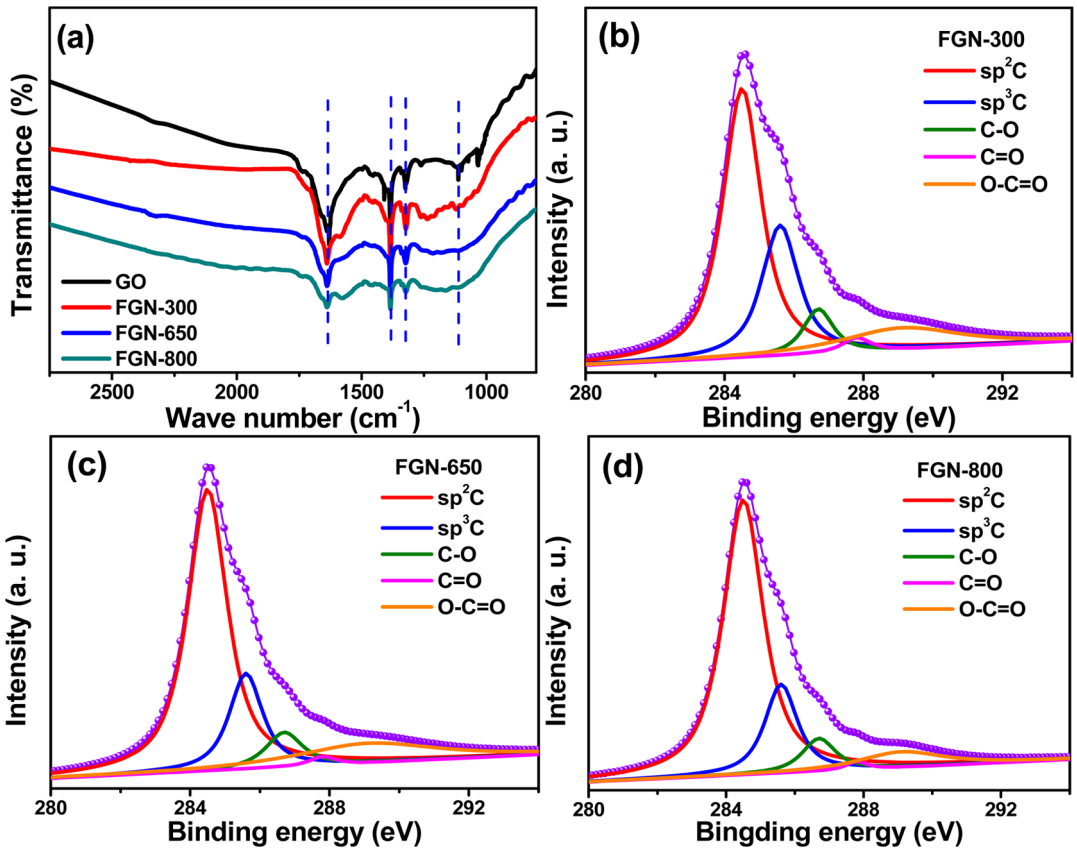

Figure 4. (a) FT-IR of GO, FGN-300, FGN-650, and FGN-800. (b−d) C 1s XPS profiles of FGN-300, FGN-650, and FGN-800.

comes from both EDLC and pseudocapacitance together according to the CV curve observation. Moreover, the CV curve of FGN-300 electrode exhibits the largest integral area, revealing that the highest capacitance among all the electrodes is mainly from the pseudocapacitance. It is worth noting that the pseudocapacitance comes from the reversible redox reactions among the hydroxyl, carbonyl, carboxyl, and lactone groups, and the related redox reactions can be expressed as follows:[25]

$$>C-OH \rightleftharpoons >C=O + H^+ + e^- \quad (1)$$

$$-COOH \rightleftharpoons -COO + H^+ + e^- \quad (2)$$

$$>C=O + e^- \rightleftharpoons >C-O^- \quad (3)$$

With the decrease of thermal treatment temperature, the amount of oxygen-containing functionalities increases, which can not only enhance the surface wettability and accessible electroactive surface area, but also provide high pseudocapacitance.

Instead of a typical rectangular shape, a well remarkable region of reversible pseudofaradaic reactions is observed at *ca.* −0.7 V for the CV curves of FGN-300 electrode at different scan rates (Figure 6a). Moreover, the obvious oxidation−reduction peaks and nonlinear characteristics of the charge/discharge curves of FGN-300 (Figure 6b) exhibit both EDLC and pseudocapacitive performance. Figure 6c presents the correlation of the gravimetric capacitances with the current densities for FGN-300, FGN-650, FGN-800, thermal exfoliated graphene sheet (TEGS), and RGO. FGN-300 exhibits the highest capacitance of 456 F g^{-1} at a current density of 0.5 A g^{-1}, much higher than RGO (181 F g^{-1}), TEGS (230 F g^{-1}),[12] FGN-650 (163 F g^{-1}), and FGN-800 (145 F g^{-1}). As the content of oxygen containing functionalities for FGN-800 sample is rather low, we believe the capacitance of the FGN-800 electrode mainly comes from the EDLC. Therefore, through deducting it from the total capacitance, the additional pseudocapacitance from oxygen-containing functionalities for FGN-300 is about 311 F g^{-1} (Figure S5, Supporting Information). Although the interfacial charge transfer resistance of FGN-300 electrode is not as small as those of FGN-650 and FGN-800 electrodes, the value of resistance between electrode material and electrolyte for FGN-300 is rather lower than others, indicating greatly improved surface wettability (Figure S6, Supporting Information). The high specific capacitance of the FGN-300 electrode can be attributed to the greatly improved surface area with more wrinkles on graphene sheets and considerable oxygen-containing functionalities, guaranteeing the contribution of EDLC and pseudocapacitance to the total capacitive performance. Notably, the capacitance obtained for FGN-300 is also highly comparable to and even much higher than previous reports on graphene[26] and oxygen-containing functionalized

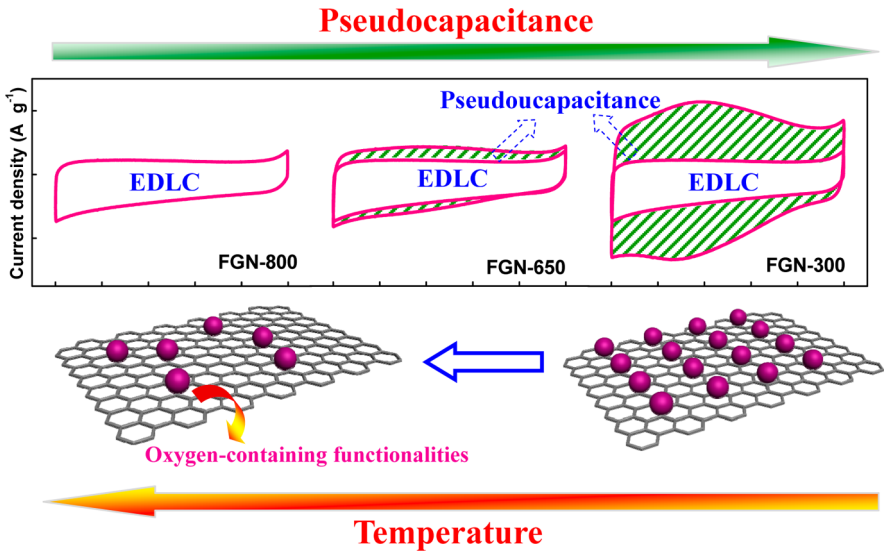

Figure 5. Illustration of the relationship between thermal temperature and pseudocapacitance.

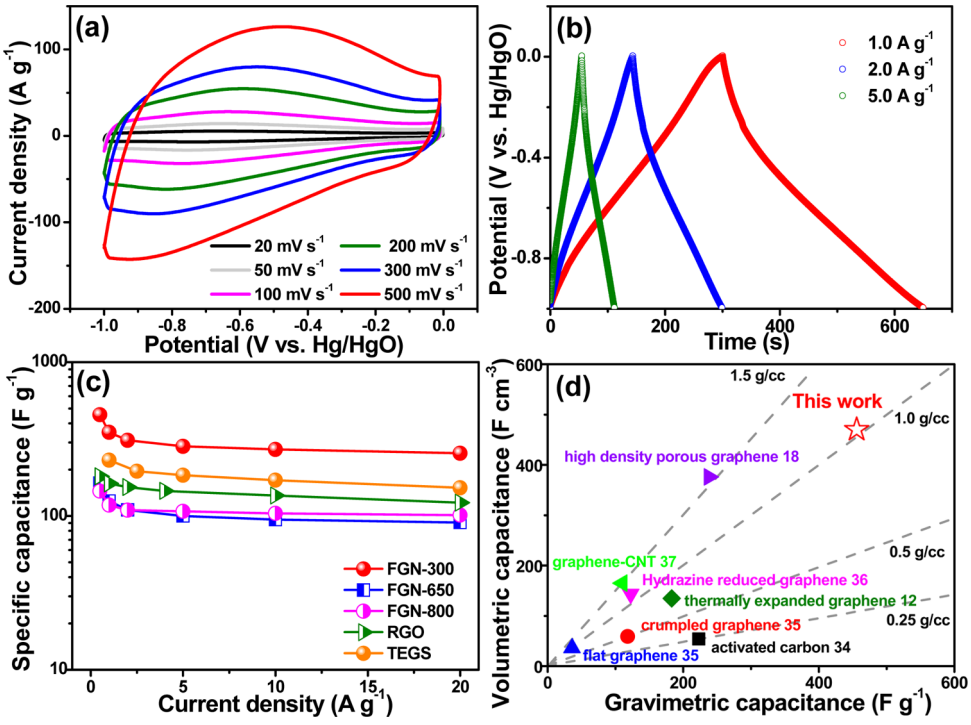

Figure 6. (a) CV curves of FGN-300 electrode at the scan rates from 20 to 500 mV s^{-1} (b) Charge/discharge curves of FGN-300 electrode at different current densities in the potential range of −1 and 0 V and (c) gravimetric capacitance of FGN-300, FGN-650, FGN-800, TEGS,[12] and RGO[36] electrodes at the current densities from 0.5 to 20 A g^{-1}. (d) Comparison of the volumetric and gravimetric capacitances of FGN-300 electrode with other carbon electrodes in aqueous electrolytes at various particle densities.

graphenes.[27−29] Since volumetric performance is also an important parameter measuring the performances of energy storage devices in practical applications,[30,31] we have also calculated the volumetric capacitance of the obtained materials according to the following equation:

$$C_v = C_g \rho \quad (4)$$

where C_v is the volumetric capacitance, C_g is the gravimetric capacitance and ρ is the particle density.[32,33] According to the obtained density of 1.03 g cm^{-3}, FGN-300 has an ultrahigh volumetric capacitance up to 470 F cm^{-3}, almost 3.3 times higher than RGO, to the best of our knowledge, which is the highest value so far reported for carbon materials in aqueous electrolytes (Figure 6d, Table S2, Supporting Information).[12,18,34−37]

In order to further demonstrate the superior electrochemical performance of the FGN-300 electrode, we assembled symmetric supercapacitors using FGN-300

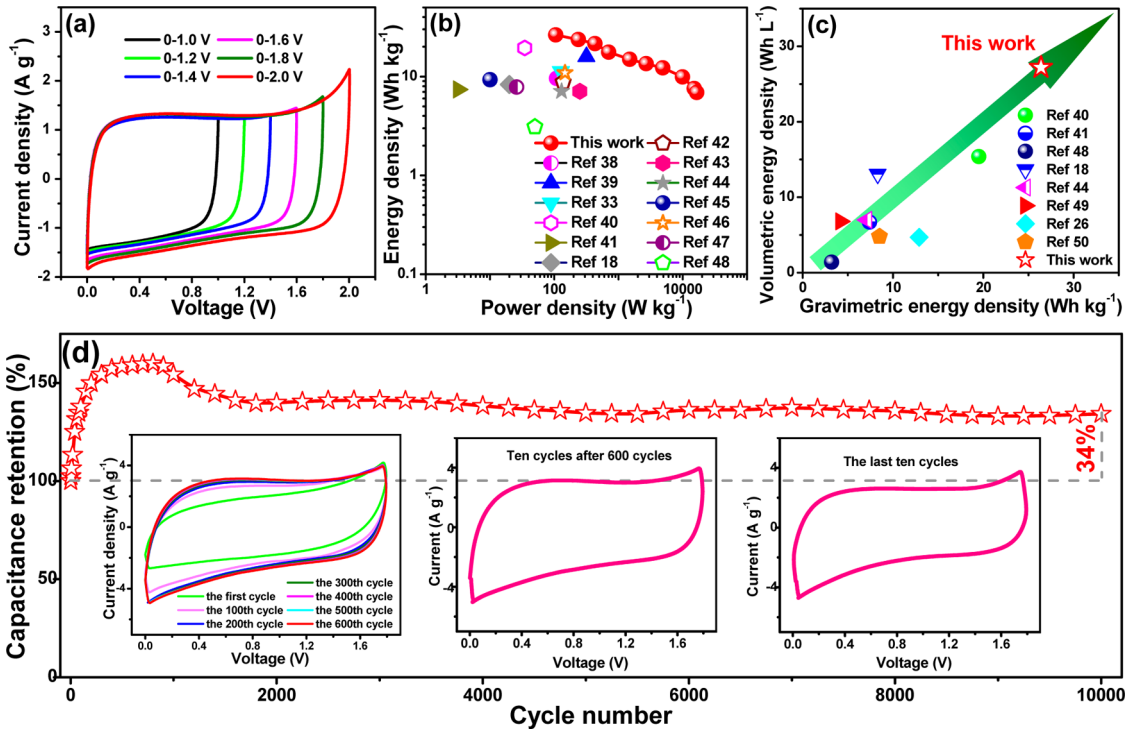

Figure 7. (a) CV curves of FGN-300//FGN-300 symmetric supercapacitor measured in different voltage windows at 50 mV s^{-1}. (b) Ragone plot of FGN-300 and other carbon-based symmetric supercapacitors. (c) Comparison of the volumetric and gravimetric energy densities of different assembled symmetric supercapacitors using carbon electrode materials in aqueous electrolytes. (d) Cycling stability of the symmetric supercapacitor after 10 000 cycles at 200 mV s^{-1}. The inset shows the CV curves with the selected cycles.

electrodes in 1 mol L^{-1} Na_2SO_4 aqueous electrolyte. Figure 7a exhibits the CV curves of FGN-300//FGN-300 symmetric supercapacitor operated in different voltage windows at 50 mV s^{-1}. There is no obvious increase of anodic current even at 1.8 V, meaning that the electrolyte is stable. Moreover, CV curves of the symmetric supercapacitor at different scan rates of 20, 50, 100, 200, and 500 mV s^{-1} are shown in Figure S7a (Supporting Information). All the CV curves display rectangular-like shape, indicating an ideal capacitive behavior. More interestingly, there is no obvious distortion even at very high scan rate of 500 mV s^{-1}, suggesting a fast charge/discharge stability and excellent rate capability. The capacitance performance of the symmetric supercapacitor was also calculated and shown in Figure S7b (Supporting Information). The capacitance is 58.6 F g^{-1} at 2 mV s^{-1} in 1 M Na_2SO_4 electrolyte. It is well-known that energy density (*E*) and power density (*P*) are two vital factors to characterize the electrochemical performance of the supercapacitor devices. Therefore, *E* and *P* have been calculated from the CV curves at various scan rates according the following equations:

$$E = 0.5CV^2 \quad (5)$$

$$P = E/t \quad (6)$$

where *C* (F g^{-1}) is the capacitance of the symmetric supercapacitor and *t* is the discharge time (s). The Ragon plot of the symmetric supercapacitor is shown in Figure 7b. The FGN-300//FGN-300 symmetric supercapacitor exhibits an energy density of 26.4 Wh kg^{-1}, higher than previous reported carbon-based symmetric supercapacitors in aqueous electrolytes.[18,33,38−48] Even at a power density of 16.6 kW kg^{-1}, the cell also delivers a high energy density of 6.9 Wh kg^{-1}.

Figure 7c shows the comparison of the volumetric and gravimetric energy densities of different assembled symmetric supercapacitors using carbon electrode materials in aqueous electrolytes. More interestingly, the FGN-300//FGN-300 symmetric supercapacitor also exhibits an ultrahigh volumetric energy density of 27.2 Wh L^{-1}, which is among the highest values for carbon materials reported in aqueous electrolytes.[18,26,40,41,44,49,50] The electrochemical stability of the symmetric supercapacitor was also measured by repeating CV tests for 10 000 cycles at 200 mV s^{-1} as shown in Figure 7d. It is worth noting that the capacitance is increased to 162% after 600 cycles, which may be attributed to the increased available active sites during the cycling process. The decrease after 1000 cycles is mainly probably by the decomposition of the unstable functionalities.[1] More importantly, there is still 134% capacitance retention after 10 000 cycles, demonstrating reversible redox reactions and rather stable oxygen-containing functionalities. Moreover, we have also tested the cycling performance at 20 mV s^{-1} for 5000 cycles (Figure S8, Supporting Information); the capacitance retention ratio exhibits the same tendency as the one measured at

200 mV s^{-1}. After the cycling test, the sample still remains its original morphology (Figure S9, Supporting Information), meaning a stable structure for FGN-300. The superior electrochemical performances of the FGN-300 electrode can be ascribed to its unique morphology, high surface area, and surface chemistry. First, $Mg(OH)_2$ template can efficiently inhibit the restacking of graphene sheets as "spacers" during the thermal-treatment process, resulting in high surface area and low pore volume. Second, there are numerous "footprints" remaining on the surface of sheets after the removal of the template, which can act as ion-buffering reservoirs that greatly facilitate the fast transportation of electrolyte ions to the surface of internal surface during the charge/discharge process. Finally, a large amount of oxygen-containing functionalities remaining on graphene sheets can not only improve the surface wettability of the electrode in electrolyte, but also provide an additional pseudocapacitance, resulting in greatly enhanced capacitance performance. More importantly, FGN-300 has high gravimetric capacitance and low pore volume, resulting in both competitive volumetric capacitance and energy density. Therefore, such kind of material with outstanding electrochemical performances, as well as green and facile fabrication, should have significant importance for both academic and industry communities.

CONCLUSIONS

In summary, we have demonstrated a template-assisted strategy for the synthesis of functionalized graphene *via* low temperature (300 °C) treatment of GO with a slow heating rate. This strategy not only enables graphene to form a dented structure without serious aggregation, but also allows the preservation of the stable oxygen-containing functionalities. Because of its highly accessible surface area and stable oxygen-containing functionalities, the obtained functionalized graphene exhibits an excellent volumetric capacitive performance as high as 470 F cm^{-3}, which is the highest volumetric capacitance so far reported for carbon materials in aqueous electrolytes, as well as superior cycle stability and ultrahigh volumetric energy density (27.2 Wh L^{-1}). Therefore, this novel route is simple and effective for large-scale production of graphene material that it is expected to greatly promote the development of high volumetric performance supercapacitors where space is limited.

EXPERIMENTAL SECTION

Synthesis of GO. GO was synthesized by the modified Hummers method from natural graphite (Qingdao Graphite Company).[9] Briefly, natural graphite powder (5 g), $K_2S_2O_8$ (2.5 g), and of P_2O_5 (2.5 g) were stirred in 15 mL of H_2SO_4 at 80 °C for 4.5 h and washed several times and dried in air overnight. Then $KMnO_4$ (15 g) was slowly added to the graphite powder solution with 115 mL of H_2SO_4 at 0 °C. After vigorous stirring at 36 °C for 2 h, 230 mL of distilled water was added at 0 °C, and the solution was stirred at 36 °C for additional 2 h. The oxidation step was completed by the addition of 700 mL of distilled water and 12.5 mL of H_2O_2 solution (35%). The GO solution (brown color) was washed and filtrated with 1000 mL of HCl (10%). Finally, the GO was dispersed in distilled water (10 mg mL^{-1}) and dialyzed for 2 weeks.

Synthesis of $Mg(OH)_2$ Template. The purchased MgO powder (4 g) was added into 500 mL of distilled water and followed by ultrasonication for 1 h. Then the dispersion was placed into a reflux apparatus and boiled for 24 h. After centrifugation and freeze-drying, $Mg(OH)_2$ was obtained.

Synthesis of FGN-300. The as-prepared $Mg(OH)_2$ (2 g) was dispersed in 200 mL of distilled water, and the GO dispersion was dropped into the above solution after ultrasonication for 1 h. After the mixture was stirred for 5 h, the mixture was filtrated and placed in a freeze drier. Then the powder was sealed in a quartz tube and heated at 300 °C for 2 h in a nitrogen atmosphere with a heating rate of 3 °C min^{-1}. The FGN-300 was obtained after hydrochloric acid treatment. FGN-650 and FGN-800 were also obtained using the same method and treated at 650 and 800 °C, respectively. In addition, TRG was also prepared without the use of $Mg(OH)_2$ template for comparison.

Material Characterization. The microstructure and morphology were characterized by SEM (Hitachi S-4800) and TEM (JEOL JEM2010). XRD measurement was conducted with Cu Kα radiation (λ = 0.15406 nm) to determine the crystallographic structures of the materials. The N_2 adsorption−desorption isotherms of the samples were performed at 77 K using NOVA 2000 (Quantachrome, USA), and the specific surface area was calculated from the BET plot of the N_2 adsorption isotherm. Thermogravimetric analysis was conducted on a PerkinElmer Diamond thermal analyzer. Raman spectra were recorded to analyze the defective nature of the materials with a Jobin-Yvon HR800 Raman spectrometer with 457.9 nm wavelength incident laser light. Infrared spectra were recorded to reflect the initial changes in the surface chemical bonding as well as the covalent grafting behavior of the hybrids on a VERTEX 70 FT-IR spectrometer (Bruker) in the frequency range 4000−500 cm^{-1}, and an XPS system (ESCALab MKII) was used to determine the surface characteristics of materials. The electrical conductivity of the samples was measured by a two-probe method. Atomic force microscopy (AFM) image was obtained on a Digital Instrument Nanoscope IIIA AFM.

Electrochemical Measurements. The electrochemical performances were first carried out on CHI 660C electrochemical station using a three-electrode system, which Hg/HgO, Pt foil, and the as-prepared materials were used as the reference, counter, and working electrodes, respectively. And two-electrode system was also employed to further investigate the performance of the electrodes. The working electrode was composed of 75 wt % of the prepared material, 20 wt % of carbon black, and 5 wt % of polytetrafluoroethylene (PTFE) binder, which were mixed together in ethanol and pressed onto nickel foam current collector. The typical mass loading on one electrode was between 2.9 and 3.1 mg cm^{-2}. CV and galvanostatic charge−discharge measurements were conducted in the potential range of −1 to 0 V in 6 mol L^{-1} KOH aqueous solution, and the specific capacitances were calculated from the discharge curves at various current densities. The capacitances of the symmetric supercapacitors were calculated according the CV curves at different scan rates based on the following equation:

$$C = \int IdV/m\upsilon V \qquad (7)$$

where I is the response current density, V is the potential, υ is the potential scan rate, and m is the weight the electroactive material in the electrode.

Conflict of Interest: The authors declare no competing financial interest.

Acknowledgment. The authors acknowledge financial support from the National Science Foundation of China (51202043, 51077014, and 21003028), Fundamental Research Funds for the Central Universities, and Program for New Century Excellent Talents in University (NCET-10-0050).

Supporting Information Available: Additional information on TEM image of prepared $Mg(OH)_2$ nanosheets and specific capacitance of the assembled supercapacitor are provided. This material is available free of charge *via* the Internet at http://pubs.acs.org.

REFERENCES AND NOTES

1. Yan, J.; Wang, Q.; Wei, T.; Fan, Z. Recent Advances in Design and Fabrication of Electrochemical Supercapacitors with High Energy Densities. *Adv. Energy Mater.* **2014**, *4*, 1300816.
2. Xu, B.; Hou, S. S.; Cao, G. P.; Wu, F.; Yang, Y. S. Sustainable Nitrogen-Doped Porous Carbon with High Surface Areas Prepared from Gelatin for Supercapacitors. *J. Mater. Chem.* **2012**, *22*, 19088–19093.
3. Liu, J.; Yang, T.; Wang, D.-W.; Lu, G. Q.; Zhao, D.; Qiao, S. Z. A Facile Soft-Template Synthesis of Mesoporous Polymeric and Carbonaceous Nanospheres. *Nat. Commun.* **2013**, *4*, 2798.
4. Wu, Z. S.; Parvez, K.; Feng, X.; Müllen, K. Graphene-Based in-Plane Micro-Supercapacitors with High Power and Energy Densities. *Nat. Commun.* **2013**, *4*, 2487.
5. Zhu, Y.; Murali, S.; Stoller, M. D.; Ganesh, K. J.; Cai, W.; Ferreira, P. J.; Pirkle, A.; Wallace, R. M.; Cychosz, K. A.; Thommes, M.; *et al.* Carbon-Based Supercapacitors Produced by Activation of Graphene. *Science* **2011**, *332*, 1537–1541.
6. Lee, J. H.; Park, N.; Kim, B. G.; Jung, D. S.; Im, K.; Hur, J.; Choi, J. W. Restacking-Inhibited 3D Reduced Graphene Oxide for High Performance Supercapacitor Electrodes. *ACS Nano* **2013**, *7*, 9366–9374.
7. Yan, J.; Fan, Z.; Sun, W.; Ning, G.; Wei, T.; Zhang, Q.; Zhang, R.; Zhi, L.; Wei, F. Advanced Asymmetric Supercapacitors Based on $Ni(OH)_2$/Graphene and Porous Graphene Electrodes with High Energy Density. *Adv. Funct. Mater.* **2012**, *22*, 2632–2641.
8. Yan, J.; Fan, Z.; Wei, T.; Qian, W.; Zhang, M.; Wei, F. Fast and Reversible Surface Redox Reaction of Graphene-MnO_2 Composites as Supercapacitor Electrodes. *Carbon* **2010**, *48*, 3825–3833.
9. Byon, H. R.; Gallant, B. M.; Lee, S. W.; Shao-Horn, Y. Role of Oxygen Functional Groups in Carbon Nanotube/Graphene Freestanding Electrodes for High Performance Lithium Batteries. *Adv. Funct. Mater.* **2013**, *23*, 1037–1045.
10. Zhu, Y.; Li, L.; Zhang, C.; Casillas, G.; Sun, Z.; Yan, Z.; Ruan, G.; Peng, Z.; Raji, A.-R. O.; Kittrell, C.; *et al.* A Seamless Three-Dimensional Carbon Nanotube Graphene Hybrid Material. *Nat. Commun.* **2012**, *3*, 1225.
11. Lv, W.; Tang, D.-M.; He, Y.-B.; You, C.-H.; Shi, Z.-Q.; Chen, X.-C.; Chen, C.-M.; Hou, P.-X.; Liu, C.; Yang, Q.-H. Low-Temperature Exfoliated Graphenes: Vacuum-Promoted Exfoliation and Electrochemical Energy Storage. *ACS Nano* **2009**, *3*, 3730–3736.
12. Yan, J.; Liu, J.; Fan, Z.; Wei, T.; Zhang, L. High-Performance Supercapacitor Electrodes Based on Highly Corrugated Graphene Sheets. *Carbon* **2012**, *50*, 2179–2188.
13. Fang, Y.; Luo, B.; Jia, Y.; Li, X.; Wang, B.; Song, Q.; Kang, F.; Zhi, L. Renewing Functionalized Graphene as Electrodes for High-Performance Supercapacitors. *Adv. Mater.* **2012**, *24*, 6348–6355.
14. Park, S.; Ruoff, R. S. Chemical Methods for the Production of Graphenes. *Nat. Nanotechnol.* **2009**, *4*, 217–224.
15. Chen, P.; Xiao, T.-Y.; Qian, Y.-H.; Li, S.-S.; Yu, S.-H. A Nitrogen-Doped Graphene/Carbon Nanotube Nanocomposite with Synergistically Enhanced Electrochemical Activity. *Adv. Mater.* **2013**, *25*, 3192–3196.
16. Lukatskaya, M. R.; Mashtalir, O.; Ren, C. E.; Dall'Agnese, Y.; Rozier, P.; Taberna, P. L.; Naguib, M.; Simon, P.; Barsoum, M. W.; Gogotsi, Y. Cation Intercalation and High Volumetric Capacitance of Two-Dimensional Titanium Carbide. *Science* **2013**, *341*, 1502–1505.
17. Beidaghi, M.; Gogotsi, Y. Capacitive Energy Storage in Micro-Scale Devices: Recent Advances in Design and Fabrication of Micro-Supercapacitors. *Energy Environ. Sci.* **2014**, *7*, 867–884.
18. Tao, Y.; Xie, X.; Lv, W.; Tang, D.-M.; Kong, D.; Huang, Z.; Nishihara, H.; Ishii, T.; Li, B.; Golberg, D.; *et al.* Towards Ultrahigh Volumetric Capacitance: Graphene Derived Highly Dense but Porous Carbons for Supercapacitors. *Sci. Rep.* **2013**, *3*, 2975.
19. Ghaffari, M.; Zhou, Y.; Xu, H.; Lin, M.; Kim, T. Y.; Ruoff, R. S.; Zhang, Q. M. High-Volumetric Performance Aligned Nano-Porous Microwave Exfoliated Graphite Oxide-Based Electrochemical Capacitors. *Adv. Mater.* **2013**, *25*, 4879–4885.
20. Li, D.; Muller, M. B.; Gilje, S.; Kaner, R. B.; Wallace, G. G. Processable Aqueous Dispersions of Graphene Nanosheets. *Nat. Nanotechnol.* **2008**, *3*, 101–105.
21. Stankovich, S.; Dikin, D. A.; Piner, R. D.; Kohlhaas, K. A.; Kleinhammes, A.; Jia, Y.; Wu, Y.; Nguyen, S. T.; Ruoff, R. S. Synthesis of Graphene-Based Nanosheets *via* Chemical Reduction of Exfoliated Graphite Oxide. *Carbon* **2007**, *45*, 1558–1565.
22. Lin, Z.; Waller, G.; Liu, Y.; Liu, M.; Wong, C.-P. Facile Synthesis of Nitrogen-Doped Graphene *via* Pyrolysis of Graphene Oxide and Urea, and Its Electrocatalytic Activity toward the Oxygen-Reduction Reaction. *Adv. Energy Mater.* **2012**, *2*, 884–888.
23. Kaniyoor, A.; Baby, T. T.; Ramaprabhu, S. Graphene Synthesis *via* Hydrogen Induced Low Temperature Exfoliation of Graphite Oxide. *J. Mater. Chem.* **2010**, *20*, 8467–8469.
24. Liu, F.; Xue, D. An Electrochemical Route to Quantitative Oxidation of Graphene Frameworks with Controllable C/O Ratios and Added Pseudocapacitances. *Chem.—Eur. J.* **2013**, *19*, 10716–10722.
25. Frackowiak, E.; Beguin, F. Carbon Materials for the Electrochemical Storage of Energy in Capacitors. *Carbon* **2001**, *39*, 937–950.
26. Xiao, N.; Tan, H. T.; Zhu, J. X.; Tan, L. P.; Rui, X. H.; Dong, X. C.; Yan, Q. Y. High-Performance Supercapacitor Electrodes Based on Graphene Achieved by Thermal Treatment with the Aid of Nitric Acid. *ACS Appl. Mater. Interfaces* **2013**, *5*, 9656–9662.
27. Lin, Z. Y.; Liu, Y.; Yao, Y. G.; Hildreth, O. J.; Li, Z.; Moon, K.; Wong, C. P. Superior Capacitance of Functionalized Graphene. *J. Phys. Chem. C* **2011**, *115*, 7120–7125.
28. Sun, D. F.; Yan, X. B.; Lang, J. W.; Xue, Q. J. High Performance Supercapacitor Electrode Based on Graphene Paper *via* Flame-Induced Reduction of Graphene Oxide Paper. *J. Power Sources* **2013**, *222*, 52–58.
29. Yu, H.; He, J.; Sun, L.; Tanaka, S.; Fugetsu, B. Influence of the Electrochemical Reduction Process on the Performance of Graphene-Based Capacitors. *Carbon* **2013**, *51*, 94–101.
30. Gogotsi, Y.; Simon, P. True Performance Metrics in Electrochemical Energy Storage. *Science* **2011**, *334*, 917–918.
31. Yang, X.; Cheng, C.; Wang, Y.; Qiu, L.; Li, D. Liquid-Mediated Dense Integration of Graphene Materials for Compact Capacitive Energy Storage. *Science* **2013**, *341*, 534–537.
32. Nishihara, H.; Kyotani, T. Templated Nanocarbons for Energy Storage. *Adv. Mater.* **2012**, *24*, 4473–4498.
33. Wang, Q.; Yan, J.; Wang, Y.; Ning, G.; Fan, Z.; Wei, T.; Cheng, J.; Zhang, M.; Jing, X. Template Synthesis of Hollow Carbon Spheres Anchored on Carbon Nanotubes for High Rate Performance Supercapacitors. *Carbon* **2013**, *52*, 209–218.
34. Xia, K. S.; Gao, Q. M.; Jiang, J. H.; Hu, J. Hierarchical Porous Carbons with Controlled Micropores and Mesopores for Supercapacitor Electrode Materials. *Carbon* **2008**, *46*, 1718–1726.
35. Luo, J. Y.; Jang, H. D.; Huang, J. X. Effect of Sheet Morphology on the Scalability of Graphene-Based Ultracapacitors. *ACS Nano* **2013**, *7*, 1464–1471.

36. Yan, J.; Wei, T.; Shao, B.; Ma, F.; Fan, Z.; Zhang, M.; Zheng, C.; Shang, Y.; Qian, W.; Wei, F. Electrochemical Properties of Graphene Nanosheet/Carbon Black Composites as Electrodes for Supercapacitors. *Carbon* **2010**, *48*, 1731–1737.
37. Jung, N.; Kwon, S.; Lee, D.; Yoon, D.-M.; Park, Y. M.; Benayad, A.; Choi, J.-Y.; Park, J. S. Synthesis of Chemically Bonded Graphene/Carbon Nanotube Composites and their Application in Large Volumetric Capacitance Supercapacitors. *Adv. Mater.* **2013**, *25*, 6854–6858.
38. Wang, Q.; Yan, J.; Wei, T.; Feng, J.; Ren, Y.; Fan, Z.; Zhang, M.; Jing, X. Two-Dimensional Mesoporous Carbon Sheet-Like Framework Material for High-Rate Supercapacitors. *Carbon* **2013**, *60*, 481–487.
39. Wang, Q.; Yan, J.; Wang, Y.; Wei, T.; Zhang, M.; Jing, X.; Fan, Z. Three-Dimensional Flower-Like and Hierarchical Porous Carbon Materials as High-Rate Performance Electrodes for Supercapacitors. *Carbon* **2014**, *67*, 119–127.
40. Raymundo-Pinero, E.; Cadek, M.; Beguin, F. Tuning Carbon Materials for Supercapacitors by Direct Pyrolysis of Seaweeds. *Adv. Funct. Mater.* **2009**, *19*, 1032–1039.
41. Raymundo-Pinero, E.; Leroux, F.; Beguin, F. A High-Performance Carbon for Supercapacitors Obtained by Carbonization of a Seaweed Biopolymer. *Adv. Mater.* **2006**, *18*, 1877–1882.
42. Qie, L.; Chen, W.; Xu, H.; Xiong, X.-Q.; Jiang, Y.; Zou, F.; Hu, X.; Xin, Y.; Zhang, Z.; Huang, Y. Synthesis of Functionalized 3D Hierarchical Porous Carbon for High-Performance Supercapacitor. *Energy Environ. Sci.* **2013**, *6*, 2497–2504.
43. Yadav, P.; Banerjee, A.; Unni, S.; Jog, J.; Kurungot, S.; Ogale, S. A 3D Hexaporous Carbon Assembled from Single-Layer Graphene as High Performance Supercapacitor. *ChemSusChem* **2012**, *5*, 2159–2164.
44. Chen, L.-F.; Zhang, X.-D.; Liang, H.-W.; Kong, M.; Guan, Q.-F.; Chen, P.; Wu, Z.-Y.; Yu, S.-H. Synthesis of Nitrogen-Doped Porous Carbon Nanofibers as an Efficient Electrode Material for Supercapacitors. *ACS Nano* **2012**, *6*, 7092–7102.
45. Wang, D. W.; Li, F.; Liu, M.; Lu, G. Q.; Cheng, H. M. 3D Aperiodic Hierarchical Porous Graphitic Carbon Material for High-Rate Electrochemical Capacitive Energy Storage. *Angew. Chem., Int. Ed.* **2008**, *47*, 373–376.
46. Bao, L.; Li, X. Towards Textile Energy Storage from Cotton T-Shirts. *Adv. Mater.* **2012**, *24*, 3246–3252.
47. He, X.; Li, R.; Qiu, J.; Xie, K.; Ling, P.; Yu, M.; Zhang, X.; Zheng, M. Synthesis of Mesoporous Carbons for Supercapacitors from Coal Tar Pitch by Coupling Microwave-Assisted KOH Activation with a MgO Template. *Carbon* **2012**, *50*, 4911–4921.
48. Zhang, J.; Jiang, J.; Li, H.; Zhao, X. S. A High-Performance Asymmetric Supercapacitor Fabricated with Graphene-Based Electrodes. *Energy Environ. Sci.* **2011**, *4*, 4009–4015.
49. Xu, B.; Wu, F.; Chen, S.; Zhou, Z. M.; Cao, G. P.; Yang, Y. S. High-Capacitance Carbon Electrode Prepared by PVDC Carbonization for Aqueous EDLCs. *Electrochim. Acta* **2009**, *54*, 2185–2189.
50. Ji, J.; Zhang, L. L.; Ji, H.; Li, Y.; Zhao, X.; Bai, X.; Fan, X.; Zhang, F.; Ruoff, R. S. Nanoporous $Ni(OH)_2$ Thin Film on 3D Ultrathin-Graphite Foam for Asymmetric Supercapacitor. *ACS Nano* **2013**, *7*, 6237–6243.